Available online at www.sciencedirect.com
ScienceDirect
International Journal of Thermal Sciences 47 (2008) 1263–1275
International Journal of Thermal Sciences
www.elsevier.com/locate/ijts

Structures of supercavitating multiphase flows

Xiangbin Li [a], Guoyu Wang [a,*], Mindi Zhang [a], Wei Shyy [b]

[a] *Department of Thermal Energy Engineering, Beijing Institute of Technology, Beijing 100081, People's Republic of China*
[b] *Department of Aerospace Engineering, University of Michigan, Ann Arbor, MI 48109, USA*

Received 15 August 2007; received in revised form 24 November 2007; accepted 24 November 2007

Available online 8 January 2008

Abstract

Supercavitation around a hydrofoil is studied based on flow visualization and detailed velocity measurement. The main purpose of this study is to offer information for validating computational models, and to shed light on the multiphase transport processes. A high-speed video camera is used to visualize the flow structures under different cavitation numbers, and a particle image velocimetry (PIV) technique is used to measure the instantaneous velocity and vorticity fields. It is shown that the cavitation structure depends on the interaction of the water–vapor mixture and the vapor among the whole supercavitation stage. As the cavitation number is progressively lowered, three supercavitating flow regimes are observed: first, fluctuating cavity with periodic vortex shedding, then, vapor and water–vapor mixture coexist inside the cavity with a turbulent wake, and finally, a cavity largely filled with vapor and with a two-phase tail and distinct phase boundaries in the wake region. Even though the overall cavity boundary seems to be quite steady, the unsteadiness of the pressure fluctuation and mass transfer process between the vapor and the two-phase regions is substantial. Furthermore, in the cavitating region, strong momentum transfer between the higher and lower flow layers takes place, resulting in a highly even velocity distribution in the core part of the cavitating region, and the lower velocity area becomes smaller and, as the cavitation number lowers, moves toward the downstream.
© 2007 Elsevier Masson SAS. All rights reserved.

Keywords: Supercavitation; High speed camera; Particle image velocimetry; Multiphase dynamics; Mass transfer

1. Introduction

Cavitation appears in various flow devices and can cause substantial, sometimes catastrophic, impact on the performance and structural integrity of them. By decreasing the cavitation numbers, four regimes can be identified: inception cavitation, sheet cavitation, cloud cavitation, and supercavitation (Wang et al. [1]). While the cavitating zone increases from discreet bubbles to contiguous domains, the cavitation generation mechanism varies from localized, instantaneous pressure drop found in inception cavitation (Rood [2]), to sustained, time dependent cavities observed in cloud and sheet cavitation (Kawanami et al. [3], Legar and Ceccio [4], Delange and Debruin [5], Kjeldsen et al. [6]). With a sufficiently low cavitation number, supercavitation occurs when the size of cavity covers the entire underwater object. Compared with other types of cavitation, in this regime, there is often a distinct interface between the main flow and the cavitating region. In recent years, supercavitation research has attracted growing interests due to its potential for vehicle maneuvering and drag reduction (Hrubes [7], Kuklinski et al. [8]). The pressure in a supercavitation region is typically considered to be uniform and equal to the saturation vapor pressure. Based on these observations, simplified analytical approaches have been proposed. For example, a free stream method based on the potential flow theory has been developed to predict the cavitation dynamics (Wu and Wang [9]). However, the potential flow analysis method does not account for the viscous and turbulent effects and is insufficient as a predictive framework.

Recently, the Navier–Stokes equations-based modeling and simulation techniques have been proposed to simulate the cavitation and supercavitation physics (e.g., Wang et al. [1], Kunz et al. [10], Senocak and Shyy [11], Wu et al. [12], Hosangadi et al. [13]). In parallel, various experimental techniques have been developed to study the flow structures and modeling issues to help guide the refinement of the cavitation models (Wang

* Corresponding author. Tel.: +86 (10) 68912395, fax: +86 (10) 68940903.
E-mail address: wangguoyu@bit.edu.cn (G. Wang).

1290-0729/$ – see front matter © 2007 Elsevier Masson SAS. All rights reserved.
doi:10.1016/j.ijthermalsci.2007.11.010

Nomenclature

c	chord length of hydrofoil	m	
P_∞	reference static pressure	$N\,m^{-2}$	
P_v	saturation vapor pressure of water	$N\,m^{-2}$	
U	reference velocity	$m\,s^{-1}$	
u	velocity component in x-direction	$m\,s^{-1}$	
v	velocity component in y-direction	$m\,s^{-1}$	
Fr	Froude number, $Fr = U/\sqrt{gc}$		
Re	Reynolds number, $Re = Uc/\upsilon$		
σ	cavitation number, $\sigma = 2(P_\infty - P_v)/(\rho U^2)$		
ω_z	z-component of the vorticity, $\omega_z = \partial v/\partial x - \partial u/\partial y$	s^{-1}	
Greek letters			
ν	kinematic viscosity	$m^2\,s^{-1}$	
ρ	density	$kg\,m^{-3}$	

et al. [1], Tassin et al. [14], Claudia and Ceccio [15], Gopalan and Katz [16]). In particular, the Particle image velocimetry (PIV) technique is frequently used. For example, Tassin et al. [14] have developed a PIV system to study the flow around the traveling bubbles in the incipient regime, and reported the near wall velocity data and gas/liquid interface location. Claudia and Ceccio [15] have studied the cavitation dynamics, the velocity field, the vorticity, strain rates, and the Reynolds stresses of the flow downstream of a cavitating shear flow using the PIV technique. Based on the PIV and high-speed photography measurements, Gopalan and Katz [16] have studied the flow structure in a closure region of an attached cavity. Recently, Foeth et al. [17] have applied the time-resolved PIV to study fully developed sheet cavitation around a hydrofoil with a varying angle of attack along the spanwise direction.

The application of PIV represents an opportunity to examine the cavitating flow in a more quantitatively comprehensive manner (Adrian [18]). Since cavitating flows consist of vapor and liquid phases, it is difficult to visualize the characteristics of an individual phase. The fluid–vapor interfaces are irregular in shape and exhibit strong time dependency. Indeed, the liquid–vapor surface can scatter the laser light, and interfere with the observation of the particle tracers due to the illumination of other particles that are not within the plane of interrogation. So, typically, the measurements are conducted around the cavity, but the flow structures inside it are still unclear. In the supercavitation regime, the cavity covers the entire solid object. In order to address the challenging issues such as drag reduction, improved understanding of the flow structure inside the cavity is critically important. In particular, in order to build a satisfactory cavitation model, the turbulent transport issues need to be addressed.

The present study focuses on multiphase fluid physics related to supercavitation to help shed light on fluid physics and to offer a basis for modeling improvement. A high speed video camera is used to observe the supercavitation development and two-phase fluid dynamics in the cavitating region. The PIV technique is used to map the instantaneous and average velocity and vorticity of supercavitating flows. In the PIV measurements, bubbles due to cavitation as well as initial entrainment of air in the water, are used as "the tracer particles" to offer improved insight into the flow structure in the supercavitating region. Various cavitation numbers have been adopted to investigate the evolution of the flow structures around and downstream of the hydrofoil, the velocity and vorticity distributions, and the time dependency of the flow field are observed.

2. Approach and set-up

2.1. Cavitation tunnel

The experiments are carried out in a closed-loop cavitation tunnel, and the schematic description is provided in Fig. 1. An axial flow pump, which is used to drive the flow in the tunnel, is located about 5 m below the test section, reducing the likelihood of pump cavitation. A tank with a volume of 5 m^3 is placed upstream of the test section to separate undesired free stream bubbles. The top of the tank is connected to a vacuum pump for controlling the pressure in the tunnel. Between the test section and the tank, a corner vane and a straightening vane are used to reduce the turbulence level of the flow in the test section. The detailed position of the hydrofoil located in the test section, with 20c in length, 5.4c in height and 2c in width, is given in Fig. 2. The flowing phenomena can be observed from three windows, one on the top, one on the bottom and one on the side, which are made of perspex for optical access.

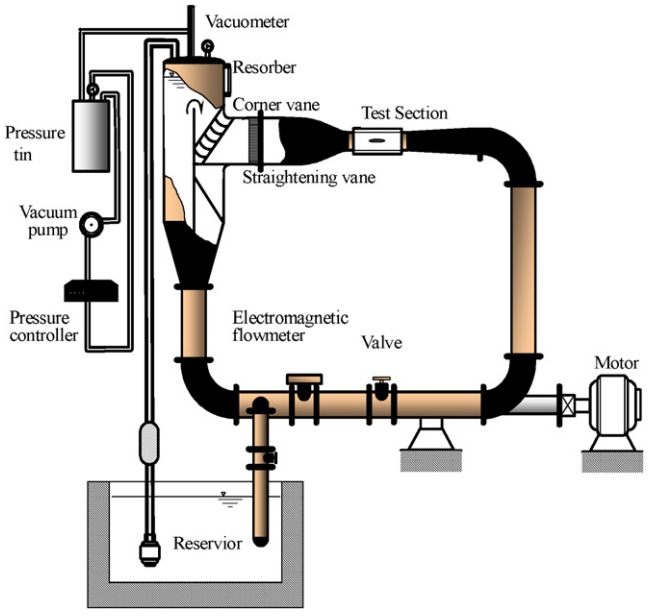

Fig. 1. Schematic of the cavitation tunnel.

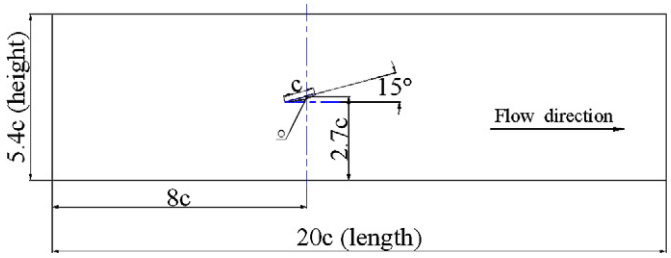

Fig. 2. Sketch of the foil's position in the test section.

To ensure the turbulent flow characteristics in the test section, the flow velocity distributions in the test section without a hydrofoil are measured by LDV (Laser Doppler Velocimetry). The distribution of the average velocities and the turbulence intensities along the spanwise direction of the test section are shown in Fig. 3. The measurement is conducted when the cavitation number is 1.29. The data are obtained at three positions: including upstream, downstream and center of the test section. The average velocities are well-distributed in the measuremented positions, and the turbulence intensity levels are smaller than 2% except the near-wall area. Since we capture data only near the mid-span area, the measured velocity distributions are limited near the middle position along Y direction; therefore, the effect from the top and bottom wall can be neglected.

The experimental conditions are maintained to within 1% uncertainty on the hydrofoil angle of incidence and 2% uncertainty on both the flow velocity and the upstream pressure. In detail, an electromagnetic flowmeter, with 0.5% uncertainty, measures the needed velocity; and a pressure transducer, with 0.25% uncertainty, monitors the upstream pressure. Together, the cavitation number can be controlled to within 5% uncertainty.

In this study, the reference velocity U is fixed at 10 m s^{-1}, the Reynolds number Re is 3.5×10^5, and the Froude number Fr is 17.

2.2. Supercavitating hydrofoil

A hydrofoil investigated by Tulin [19], as shown in Fig. 4, is adopted in the present study. A main feature of this hydrofoil is supercavitation can occur easily. The hydrofoil, with 2c in spanwise direction, is made of stainless steel, and highly surface-polished. As is clamped on the wall of the test section with a mechanical locking system, the foil can be fixed at a given angle of incidence. The suction side of the foil is mounted toward the bottom for the convenience of viewing the flowing field. The definition of incidence angle is also presented in Fig. 4.

2.3. Visualization techniques

The cavitation phenomena are documented by a high-speed digital camera (HG-LE, by Redlake), up to a rate of 10^5 frames per second (fps). In order to maintain desirable spatial resolutions, much lower recording speed is adopted. Specifically, depending on the focus of the investigation, three rates, namely, 50, 2000, and 500 fps are used in this study, respectively. The experimental setup is illustrated in Fig. 5. With the flowing field at the mid-span of the foil illuminated by a continuous laser beam sheet (LBS) from the bottom wall, the pictures are captured and transmitted to the computer in real time for post processing.

2.4. Velocity data acquisition

Also as shown in Fig. 5, a 2D-PIV system, manufactured by TSI, is composed of double-pulsed Nd:YAG laser emitting a laser sheet, a PIVCAM 10-30 CCD (Charge Coupled Device) camera with a resolution of 12 bits, 1024 × 1024 pixels collecting the instantaneous images, and one type of synchronizer providing the timing and sequencing of events. The precision of

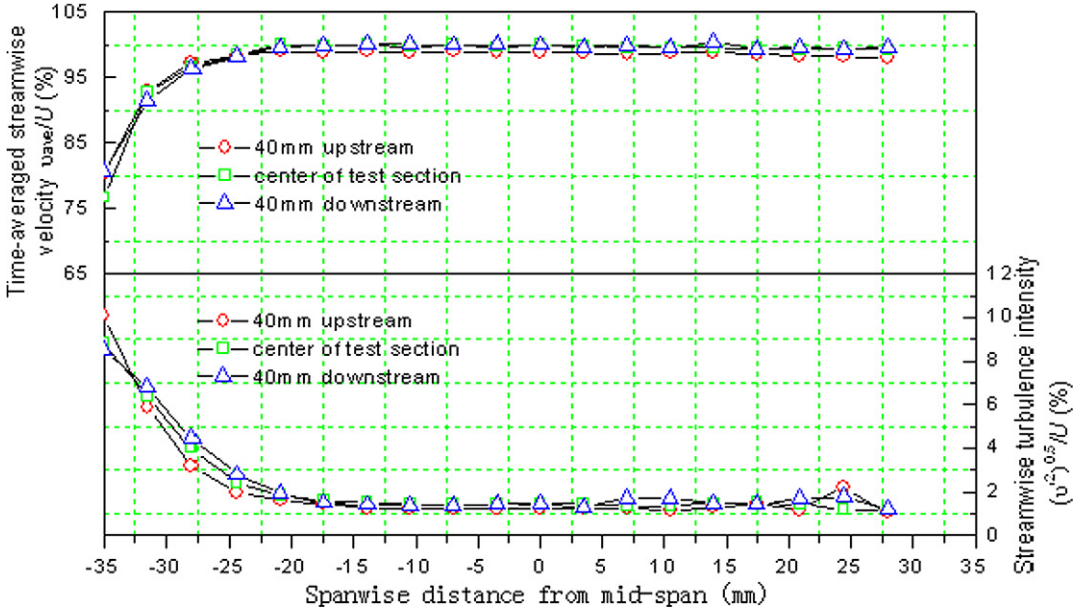

Fig. 3. Distributions of the average velocity and the turbulence intensity along spanwise direction in the test section (without a hydrofoil).

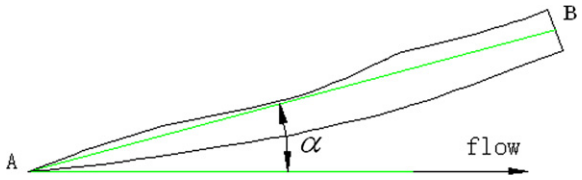

Fig. 4. Schematic of supercavitation foil.

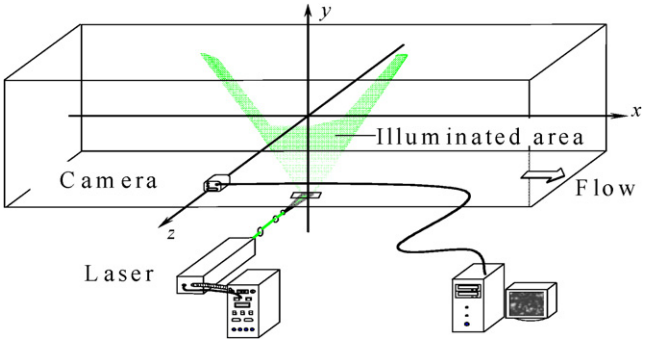

Fig. 5. Schematic of the layout of the experimental setup.

the whole system is within 0.5 ∼ 2%. The pulse laser sheet is formed with a light-guide arm and shown as a green light band (around 532 nm), with an energy of 50 mJ/pulse at a repetition rate of 30 Hz.

For two-phase flows, it's necessary to partition the velocity fields. Grünefeld et al. [20], Boëdec, and Simoëns [21] collected both images with different wavelengths using two sets of PIV systems, which combined PIV and laser-induced fluorescence (LIF). This is costly due to the additional PIV system. Furthermore, the uncertainty of measurements increases due to interference between different laser sheets, synchronization of two sets of PIV systems, and choice of two separate tracer particles. For the cavitating flows, appropriate selections of tracer particles are particularly critical because (1) the tracking capability of the tracer particles, which must be of a similar density to the liquid/gas medium and with small enough of diameters, and (2) the cavitating area is defined by irregularly-shaped and time dependent liquid–vapor interface, which can scatter the laser sheet and give incorrect interrogation information.

On the other hand, in the cavitating flows, the velocity information inside the cavity can also be captured only using the vapor bubbles as "tracer particles" (Wosnik and Milosevic [22]). In fact, the free stream carries some air bubbles and the cavitating region consists of numerous vapor bubbles. With this approach, both the cavitating flow structure and the measurement uncertainty can be assessed.

The commercial PIV-software Insight 2.0 from TSI is used to process the velocity vector fields with the interrogation areas of 32 × 32 pixels and 50% overlap in general. The images are treated with two-frame cross-correlation processing. In addition to Fast Fourier Transforms (FFT) and Gaussian algorithm for peak search, multiple filters have also been employed to remove the erroneous vectors by specifying the relative tolerance until reasonable results are obtained.

3. Results and discussions

3.1. Multiphase structures associated with supercavitation

In the present study, when the cavitation number is reduced to 0.77 or lower, at 15-degree angle-of-attack, supercavitation is attained and a relatively stable cavity covers the entire hydrofoil suction surface, extending behind the trailing edge. In the supercavitation regime, the different flow patterns appear in response to the variation of the cavitation numbers. Selected supercavitation patterns under different cavitation numbers are presented in Fig. 6. Both original flow visualization illuminated by a LBS (Fig. 6(a)) and schematic interpretations (Fig. 6(b)), drawn by an in-house feature-recognition software package, are presented. In the supercavitation regime, there is a distinct interface between water and cavitating flow regions, which is called the cavity boundary in this study. The cavitating flow patterns exhibit different characteristics in accordance with the cavitation numbers. Based on the observations, three stages are shown in the figure, that is: first, fluctuating cavity with periodical vortex shedding, then, vapor and water–vapor mixture coexist inside the cavity, followed by a turbulent wake, and finally, a cavity largely filled with vapor and with a two-phase tail and distinct phase boundaries in the wake region.

Refer to aforementioned comment on three stages, with the cavitation number of 0.77, the whole cavity is full of water and vapor mixture. As shown in Fig. 7, the flowing structures exhibit substantial temporal variations. Generated from the foil's leading (the lower vortex) and the rear blunt edge (the upper vortex), the cavitation vortices shed from the cavity tail with obvious period. The period is counted between two consecutive peak positions of the upper shedding vortices. At the time of $t = 0$ ms, the upper cavitation vortex begins to shed as the arrows indicated. An arrow also points out the shedding of the lower vortex as $t = 4$ ms. Several shedding frequencies of the vortices are listed in Table 1, according to various recording rates. The average shedding frequency—about 129 Hz, is obtained. It can be said that the first stage of supercavitation development is characterized by fluctuating cavity with periodic vortex shedding.

Further lowering the cavitation number, the cavity becomes larger and longer, and a transparent area can be observed near the hydrofoil suction surface (see, e.g., the case of $\sigma = 0.30$ in Fig. 6), which indicates that the cavity's front is largely filled with vapor. In the condition, the cavitating area consists of two parts: vapor area in the foreside of the cavity, two-phase mixture area in the rear region, and a distinct interface between the two zones can be seen. To show it more clearly, the time-evolved pictures with $\sigma = 0.30$ are given in Fig. 8, the arrows in the figure point out the interface position. Obviously, the interface location is highly unsteady, which indicates a reverse motion from two-phase mixture area to vapor area, just like the backfilling process in ventilated supercavitation (Knapp [23]). After arriving at the rearward portion of the foil at $t = 16$ ms, the interface continues to move toward the leading edge along the foil suction section until $t = 28$ ms, which shows a fully developed backfilling process. What's more, various backfilling processes

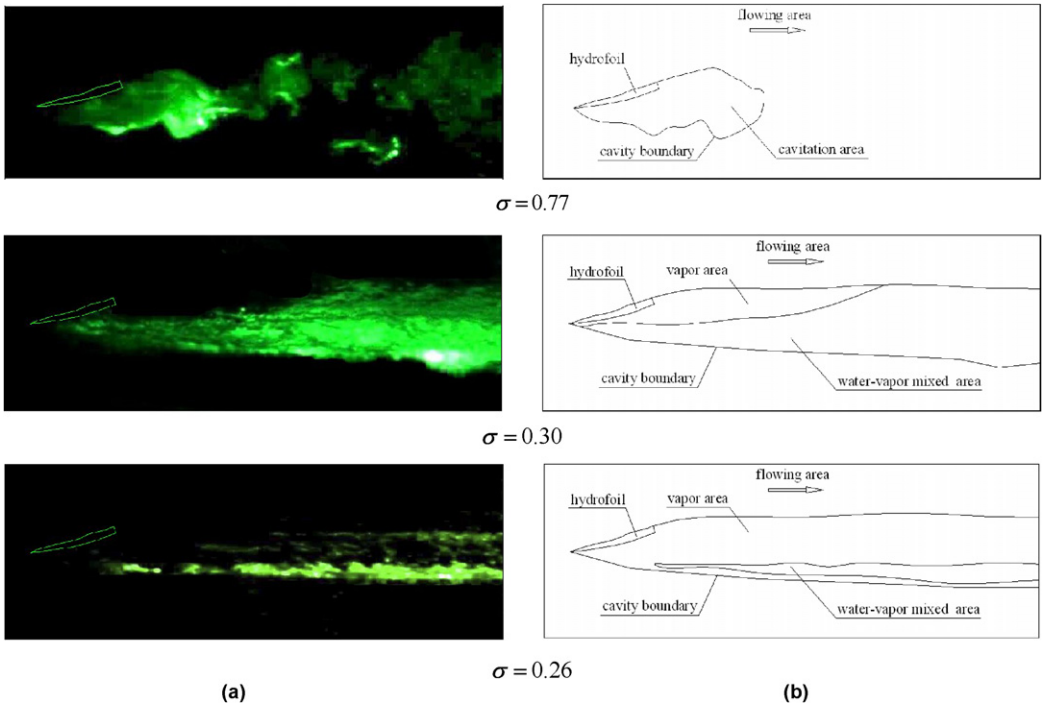

Fig. 6. Three supercavitating flow structures with different cavitation numbers. In all cases, $\alpha = 15°$. Both flow visualization and schematic interpretation are depicted.

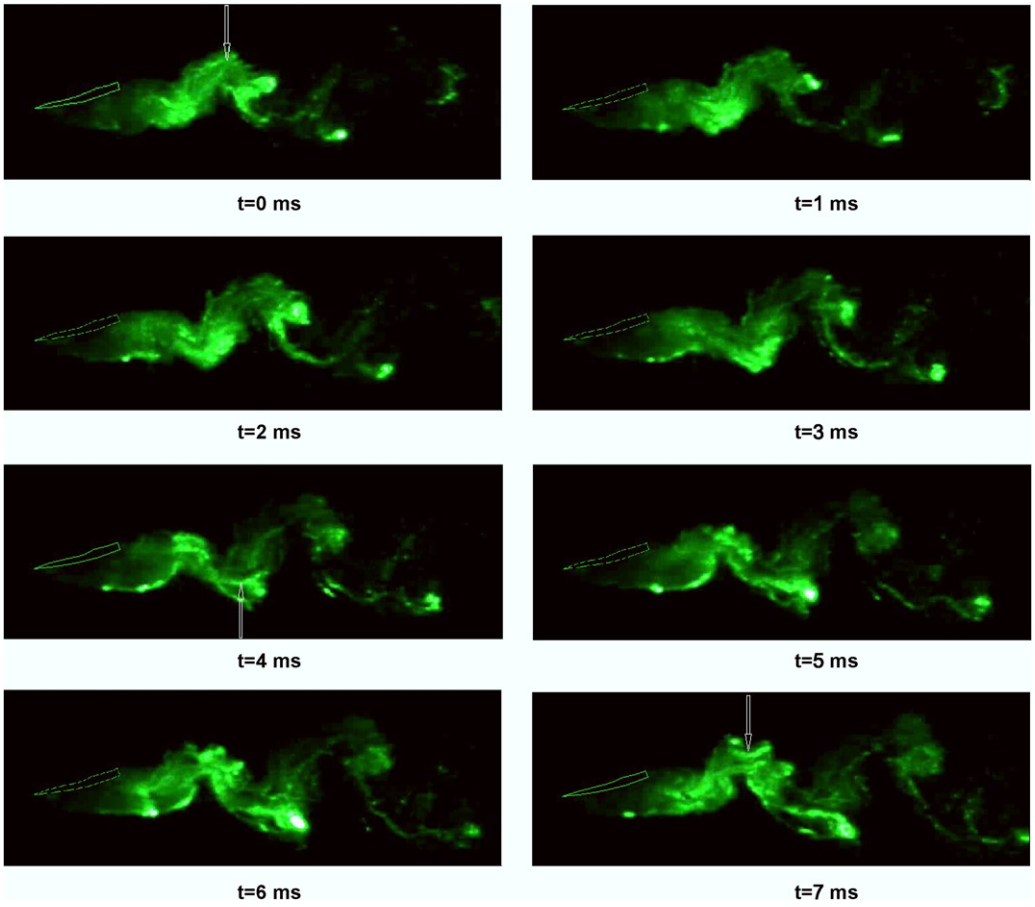

Fig. 7. Time evolution of the cavity fluctuating and the vortex shedding ($\sigma = 0.77$).

Table 1
Comparisons of observed vortex shedding dynamics

Recording rate (fps)					2000				
Shedding	133.33	117.65	142.86	153.85	125.00	105.26	142.86	117.65	133.33
Frequency (Hz)	117.65	133.33	117.65	142.86	117.65	153.85	125.00	117.65	
Average value (Hz)					129.26				
Recording rate (fps)					500				
	166.67	125.00	100.00	125.00	166.67	100.00	125.00	125.00	125.00
Shedding	125.00	125.00	166.67	100.00	125.00	166.67	125.00	100.00	166.67
Frequency (Hz)	100.00	100.00	125.00	125.00	125.00	166.67	100.00	166.67	125.00
	125.00	100.00	166.67	125.00	125.00	125.00	125.00		
Average value (Hz)					128.92				

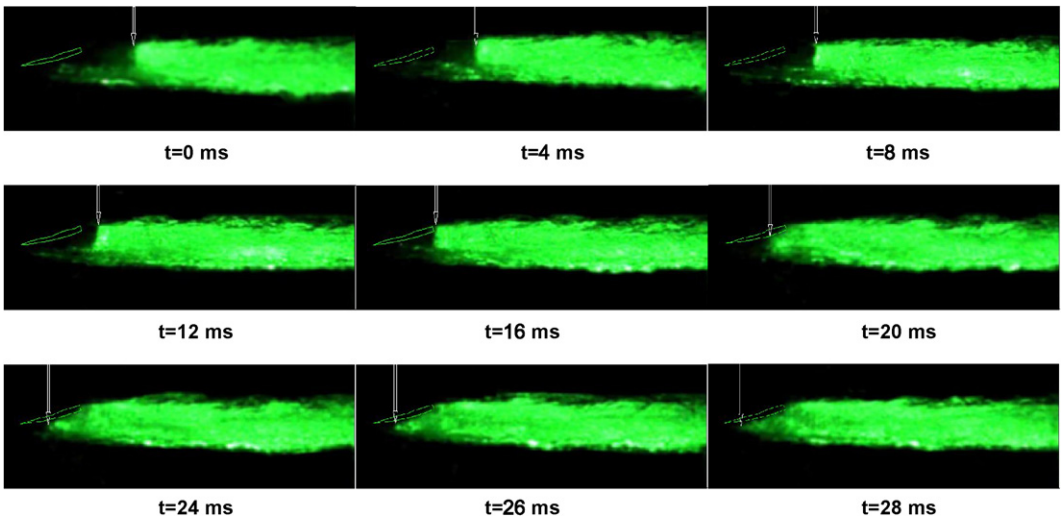

Fig. 8. Time evolution of the interface between vapor and two-phase mixture regions—1 ($\sigma = 0.30$).

can be found in the present study. As shown in Fig. 9, the interface is divided into two parts: the vertical section in upper part and the declining section in lower part. While there is a periodic backfilling in the upper region, water–vapor mixture is converted to vapor in the lower region. Furthermore, the corresponding backfilling velocities of the interface are estimated with normalized data in Fig. 10(a) and (b) respectively. Here, $t' = t/t_\infty$, t and t_∞ (c/U) are the real time and reference time respectively, and $v' = v/U^*100\%$. It can be found that the fluctuating ranges of the velocity are kept within 12–25%, i.e., the backfilling velocity occupies 12–25 percentage of the reference velocity.

Since the pressure in the transparent vapor area is essentially the same as the vapor pressure, and the pressure in the mixture region is expected to be higher, the pressure difference induces the time dependency of the interface location. When the interface moves to the left (see Figs. 8 and 9), the vapor region becomes smaller and the two-phase mixture region grows. In the process, condensation occurs in the left region, resulting in a higher pressure there. Conversely, as the interface moves to the right, the evaporation occurs, and the pressure in the left region is expected to decrease. Under supercavitation condition, even though the cavity boundary seems to be quite steady, the pressure fluctuation and unsteady mass transfer process can still be substantial inside the cavity, between the vapor and the two-phase regions. Thus, the second stage of supercavitation development can be characterized as vapor and water–vapor mixture coexist inside the cavity, followed by a turbulent wake.

When the cavitation number further decreases to 0.26, while still maintaining the angle-of-attack at 15-degree, the violent fluctuation of the interface between the vapor and the two-phase regions in the cavity disappears, the cavitation area is largely filled with vapor, and the water–vapor mixture only occupies a narrow region, as shown in Fig. 6. The time-evolved pictures are shown in Fig. 11, which exhibit similar features. The same flow pattern persists while the cavitation number is further lowered. In summary, this final stage of supercavitation development can be characterized as a vapor-filled cavity with a two-phase tail and distinct phase boundaries in the wake region.

3.2. Velocity distributions

The supercavitating and no-cavitating flow fields are measured by double-pulsed PIV images. The concerned flow region is illuminated by a laser beam sheet from the bottom window of the test section, as shown in Fig. 12, which gives a double-pulsed images when $\sigma = 0.77$. In the experiment, the interval between the image pairs is 50 μs. Based on the velocity vector data processed in Fig. 13, the following velocity and vorticity distributions can be obtained through post-processing.

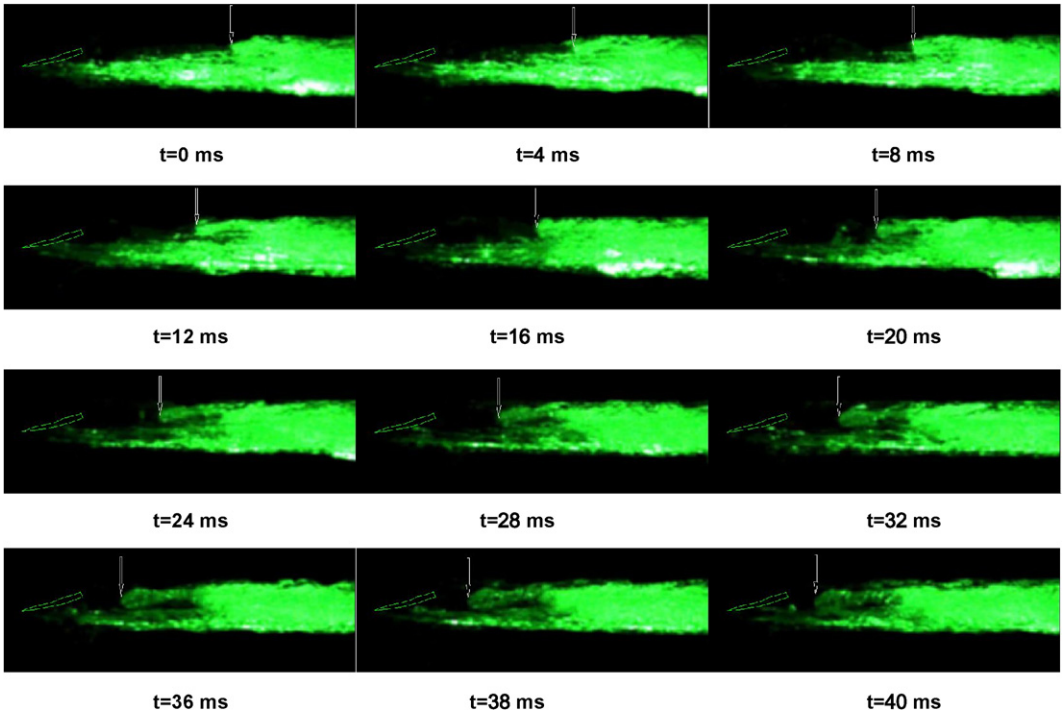

Fig. 9. Time evolution of the interface between vapor and two-phase mixture regions—2 ($\sigma = 0.30$).

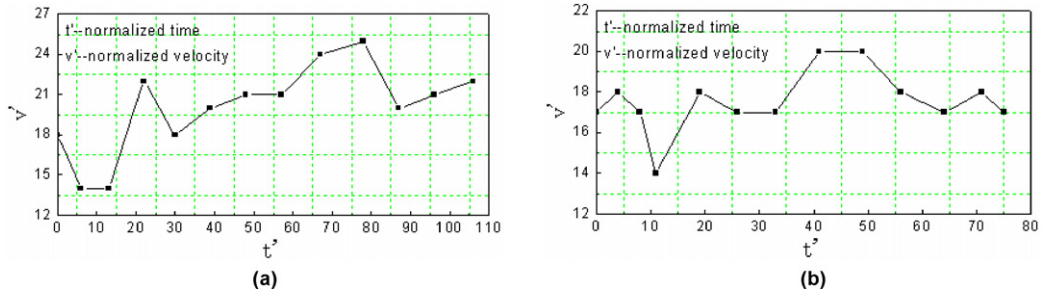

Fig. 10. Variation of backfilling velocity of the interface.

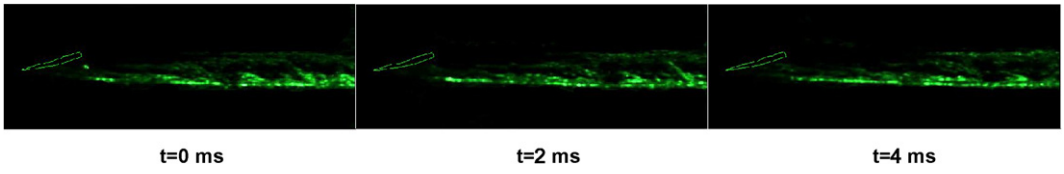

Fig. 11. Time-evolved supercavitation structures ($\sigma = 0.26$).

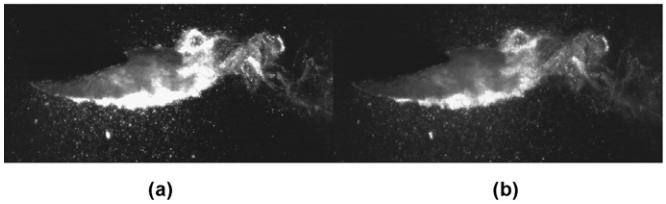

Fig. 12. Double-pulsed image pairs ($\sigma = 0.77$).

3.2.1. *Flow structures in no-cavitation condition*

The distributions of flowing fields with no cavitation are presented in Fig. 14. Fig. 14(a) shows the distribution of the velocity vectors, and Fig. 14(b) gives the distribution of the vorticity contours. The gray area indicates no laser light entered. Apparently, in the single-phase flows, the whole flowing field can be divided into two areas: (1) In the rearward portion of the foil-suction section, the velocity is much lower than that in another flow region, and extending to form a wake. Thus, this area is characterized as low velocity area. (2) In the other region except the low velocity area, no large velocity fluctuating occurs. This area is characterized as main stream (free stream) area.

The following characteristics can be observed in the aforementioned low velocity area: (a) Two vorticity bands, with positive and negative direction respectively, are formed. Time-evolved vorticity-contour distributions under no-cavitation conditions are presented in Fig. 15. It can be found the position

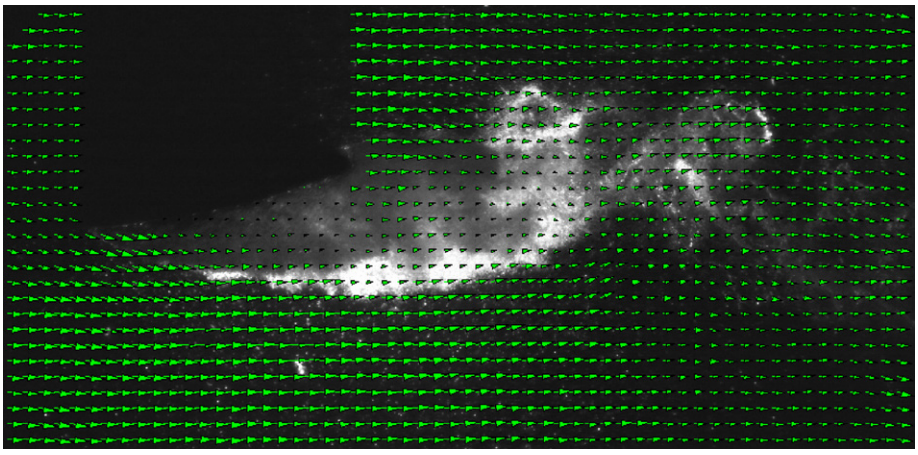

Fig. 13. The final velocity vector fields ($\sigma = 0.77$).

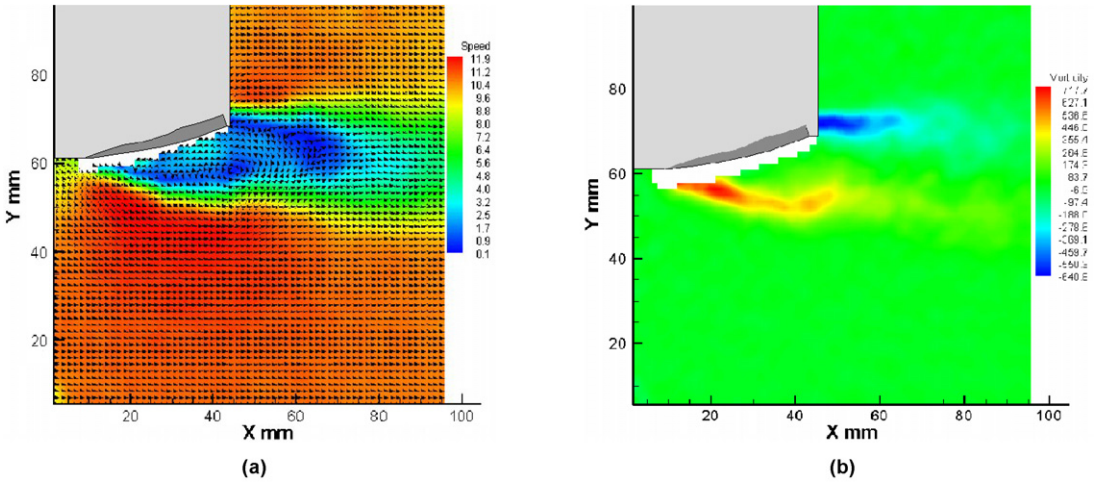

Fig. 14. Distribution of the average characteristics with no cavitation ($\sigma = 2.67$).

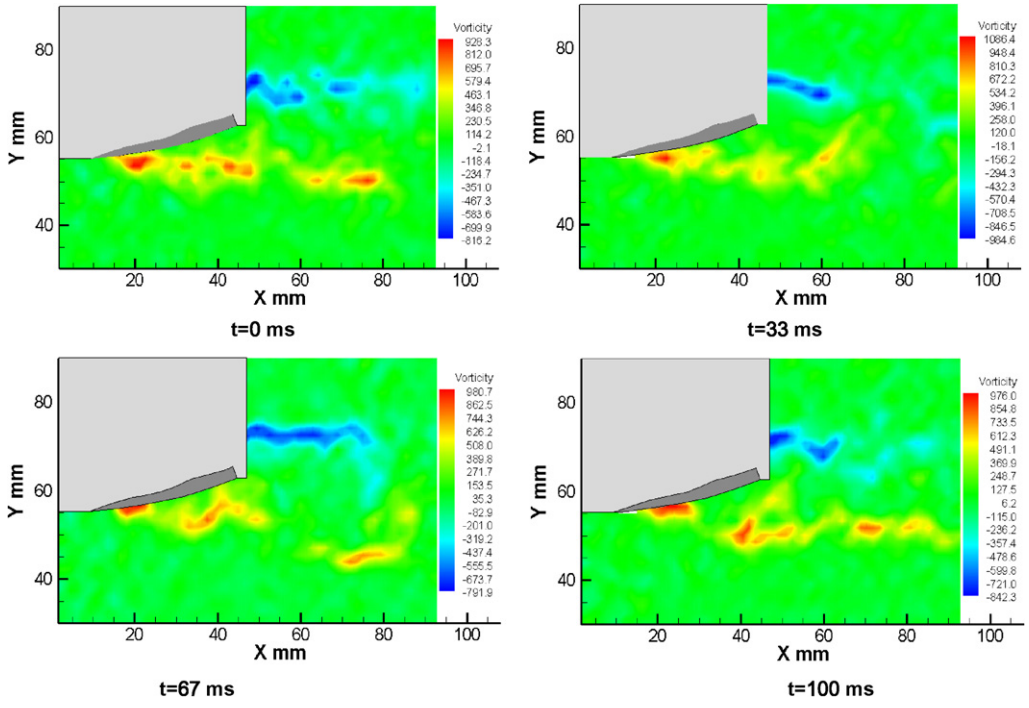

Fig. 15. Illustration of the instantaneous, z-component vorticity distribution ($\sigma = 2.67$).

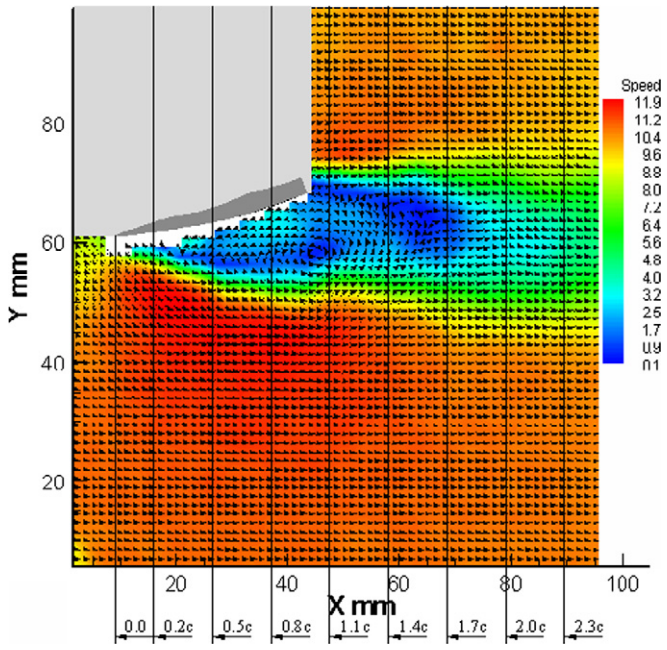

Fig. 16. Schematic of special locations ($\sigma = 2.67$).

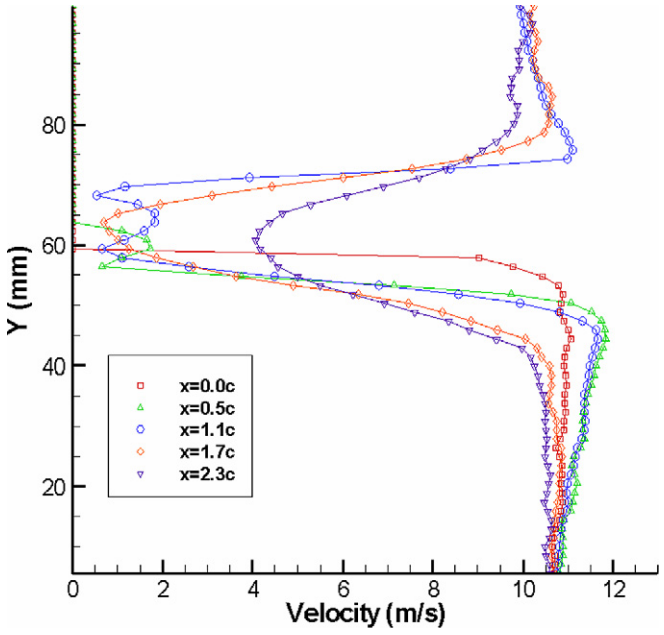

Fig. 17. Velocity distributions in various sections ($\sigma = 2.67$).

from which the vortex is formed remains unchanged, while their shape and length changes violently, which shows that the vorticity distribution of the flowing fields behaves substantial fluctuating under no cavitation condition. (b) In order to offer more quantitative information, the average velocity distributions in selected sections, as shown in Fig. 16, are provided in Fig. 17. At the positions of $x = 0.5c$ and $x = 1.1c$ near the foil suction section, there are larger velocity fluctuation, in a double-trough shape, while the wakes are quite smooth between $x = 1.7c$ and $x = 2.3c$.

3.2.2. Velocity distributions

The average velocity distributions are given in Fig. 18 for three cavitation numbers: 0.77, 0.30, and 0.26. The velocity vector plots and contours are presented in Fig. 18(a) and (b), respectively. The quantitative velocity distributions in the same sections, as shown in Fig. 16, are provided in Fig. 19. It can be seen that the velocity distributions in the cavitating regions are different from those in the bulk flows. Compared to the low velocity area in Fig. 14(a), similar characteristics are observed in the cavitation area. However, there is more uniform velocity distribution in the cavity core, as exhibited by Figs. 17 and 19, e.g., at $x = 0.5c$ and $x = 1.1c$. In summary, in the cavitating conditions, with the generation of cavities in the water–vapor two-phase flow, enhanced momentum transfer between upper and lower flow layers is induced by phase change and cavitation dynamics.

Indeed, with the cavitation number decreasing, different features can be found. As $\sigma = 0.77$, the low velocity area extends along the whole downstream field with the violent fluctuating of vortex shedding. When reducing the cavitation number, the low velocity area becomes smaller, confined between the upper and lower free streams, and the low speed fluid moves toward the rear region of the cavity.

3.2.3. Vorticity distribution

Around the interface between cavitating and no-cavitating areas, as discussed by Wang et al. [1], and confirmed by the present measurement, a shear flow region exists. The z-component vorticity distributions can be seen in Fig. 20. As expected, high levels of vorticity are observed around the cavity boundary in different cavitating conditions. The vortex bands behave with obvious stage characteristics with the decreasing of the cavitation number. Firstly, the upper and lower vortex bands approach each other with the decreasing of the cavitation number, and extend downstream. Secondly, the position in which the lower vortex band form moves back, indicating the inherent relation between the vortex band and the water–vapor mixture. What's more, the vorticity is reduced with the decreasing of the cavitation number, just as shown in Fig. 21. To further highlight the cavitation dynamics, time-evolved vorticity-contour distributions with three cavitation numbers $\sigma = 0.77$, $\sigma = 0.30$ and $\sigma = 0.26$ are presented in Figs. 22–24, respectively. With the cavitation number $\sigma = 0.77$, as shown in Fig. 22, the vortex bands almost centralize along the wake flow close to the foil, although much shorter than that with the cavitation number $\sigma = 2.67$. With the cavitation area extending to the whole test region, the vortex bands become much longer and move to the right end as shown in Fig. 23. In this stage, corresponding to the traverses of the interface between the vapor phase and the mixture phase, changes of the vortex bands area are observed. At the final stage as shown in Fig. 24, the vortex bands appear steady with less shedding.

3.3. Computational and modeling issues

Regarding future directions, various issues related to supercavitation should be addressed using combined computational modeling and experimental approaches. Specifically, the structures of the three supercavitating flow regimes need to be clari-

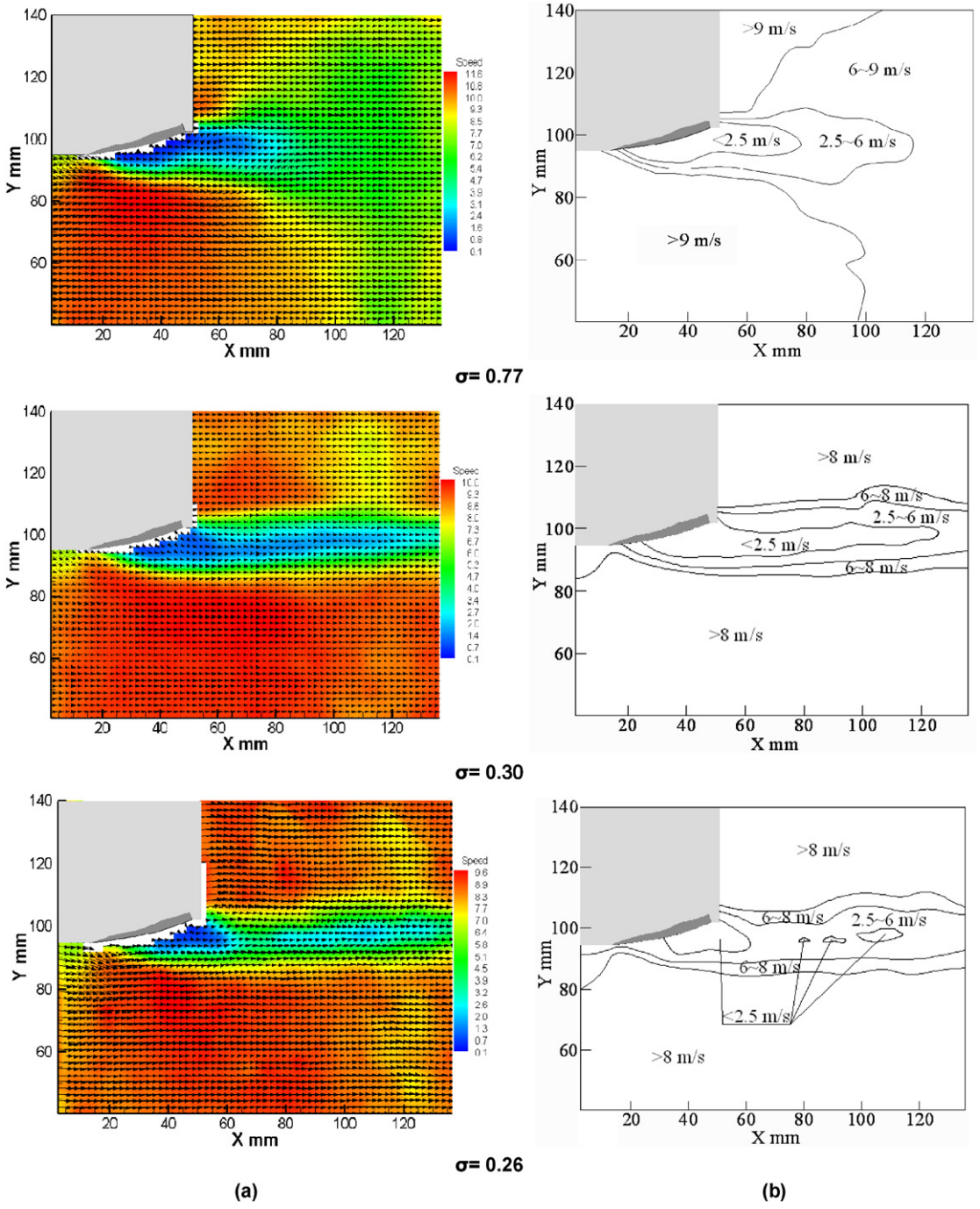

Fig. 18. Velocity distribution under different cavitation numbers.

fied. For example, the vortex shedding frequency and the mechanism about the instability of the interface between the vapor and the two-phase mixture are not well understood. These aspects seem to be closely related to the interplay between the supercavitation and the vortex dynamics. A multi-scale model can be fruitful for treating bubbly flows for finely structured cavitating flows. Turbulence modeling needs to be refined to handle two-phase and compressibility effects. In particular, capabilities for handling the following characteristics are not adequately developed:

i. substantial departure from equilibrium between production and dissipation of the turbulent kinetic energy,
ii. turbulence-enhanced mass transfer across the liquid–vapor interface,
iii. momentum transfer between liquid and vapor phases.

The conventional Reynolds-averaged Navier–Stokes approach, even with nonequilibrium effects, may not be adequate to address these challenges. Other than large eddy simulations (LES) and direct numerical simulations (DNS), a hybrid approach such as filter-based RANS model can be useful. As

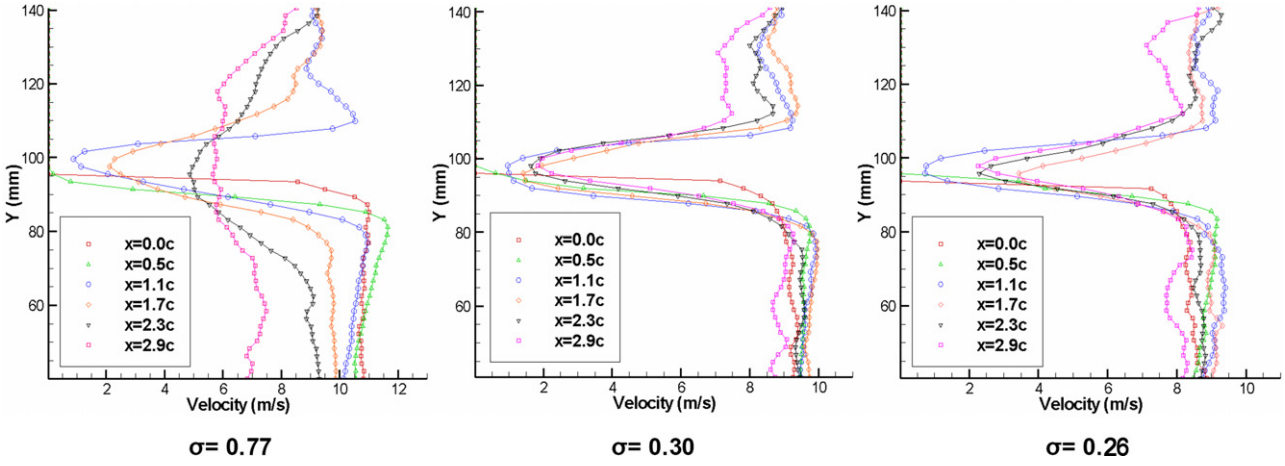

Fig. 19. The average velocity distributions in special sections.

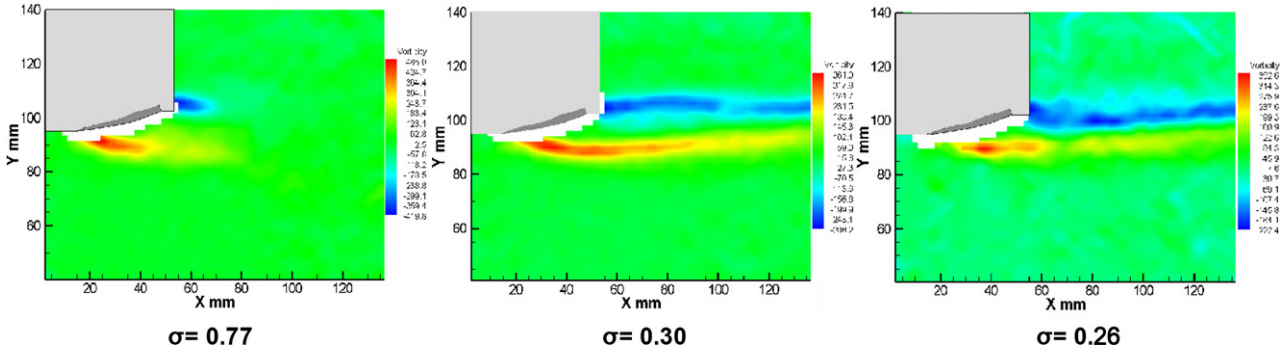

Fig. 20. The z-component average vorticity distribution in supercavitation conditions.

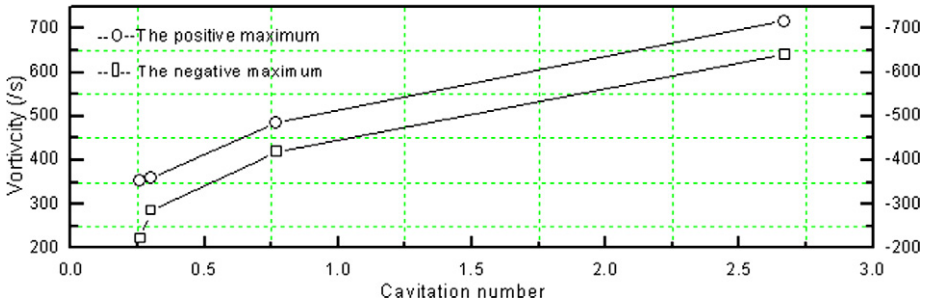

Fig. 21. The z-component average vorticity distribution under various cavitation numbers.

presented by Johansen et al. [24], and partially evaluated by Wu et al. [12] for cavitating flow simulations, the predictive capability of the current RANS-based engineering turbulence closure, conditional averaging can be adopted for the Navier–Stokes equation, with one more parameter, based on the filter size, introduced into the turbulence model. There are great opportunities to make progress in the modeling and simulation of cavitating flows.

4. Conclusions

The multiphase dynamics, velocity, and vorticity distributions associated with supercavitation are presented. The following is a summary of the main findings:

(1) The cavitation structure depends on the interaction of the water–vapor mixture and the vapor among the whole supercavitation stage. Distinct flow regimes are observed with the decreasing cavitation numbers: (a) first, fluctuating cavity with periodic vortex shedding; (b) then, vapor and water–vapor mixture coexist inside the cavity, followed by a turbulent wake; and (c) finally, a cavity largely filled with vapor and with a two-phase tail and distinct phase boundaries in the wake region.

(2) The interface between the vapor and the two-phase mixture exhibits substantial unsteadiness, indicating frequent mass transfer processes occurring inside the cavity.

(3) In the supercavitating region, strong momentum transfer between higher and lower flow layers takes place; velocity

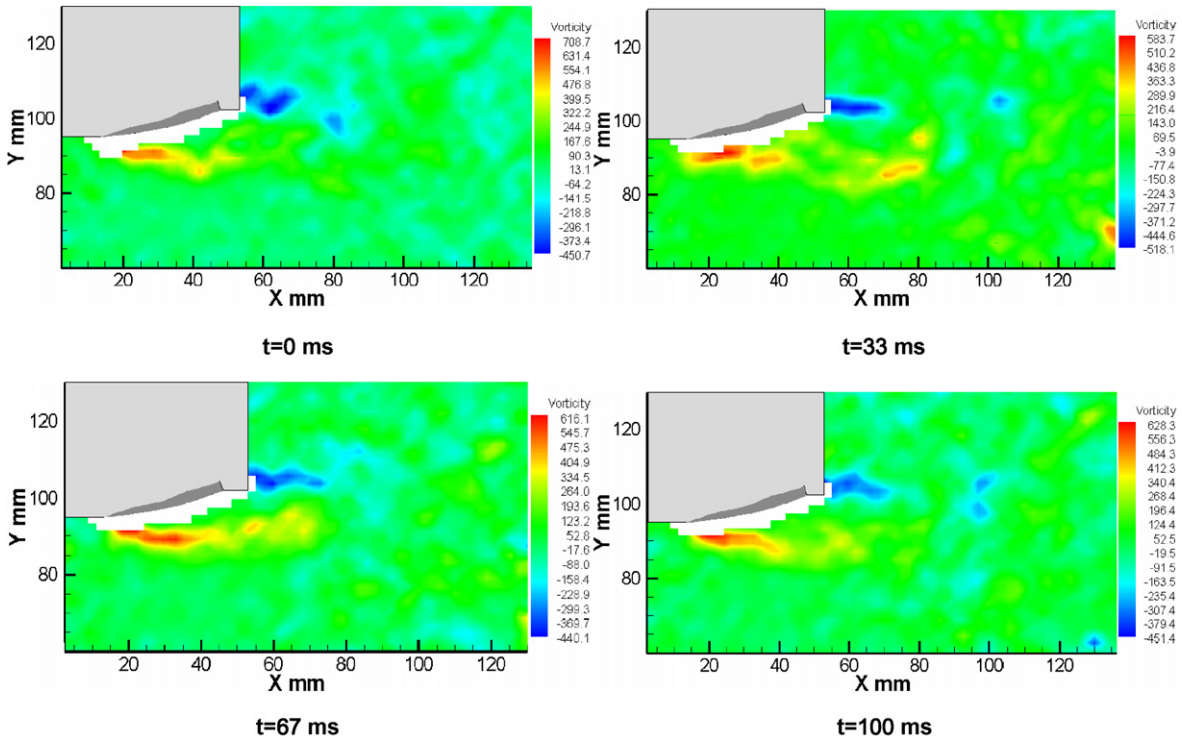

Fig. 22. Illustration of the instantaneous, z-component vorticity distribution ($\sigma = 0.77$).

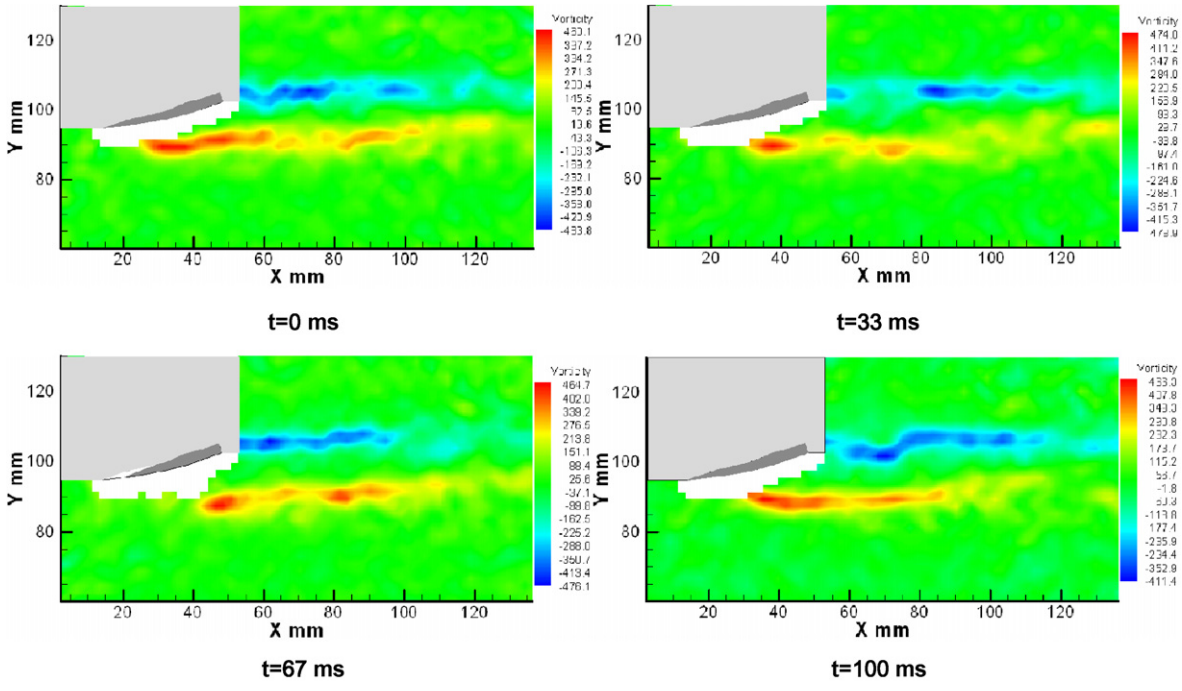

Fig. 23. Illustration of the instantaneous, z-component vorticity distribution ($\sigma = 0.30$).

distribution appears even in the core part of the cavitating region, and the lower velocity area becomes smaller and, as the cavitation number lowers, moves toward the downstream.

(4) Around the cavity boundary of the two-phase mixture is a shear layer flow, with a pair of vortex bands formed. The development of the lower vortex band is related with the distribution of the water–vapor mixture. Also, the vorticity reduces with the decreasing of the cavitation number.

Various issues related to supercavitation including the structures of the three supercavitating flow regimes, the vortex shedding frequency, and the mechanism about the instability of the interface between the vapor and the two-phase mixture await to

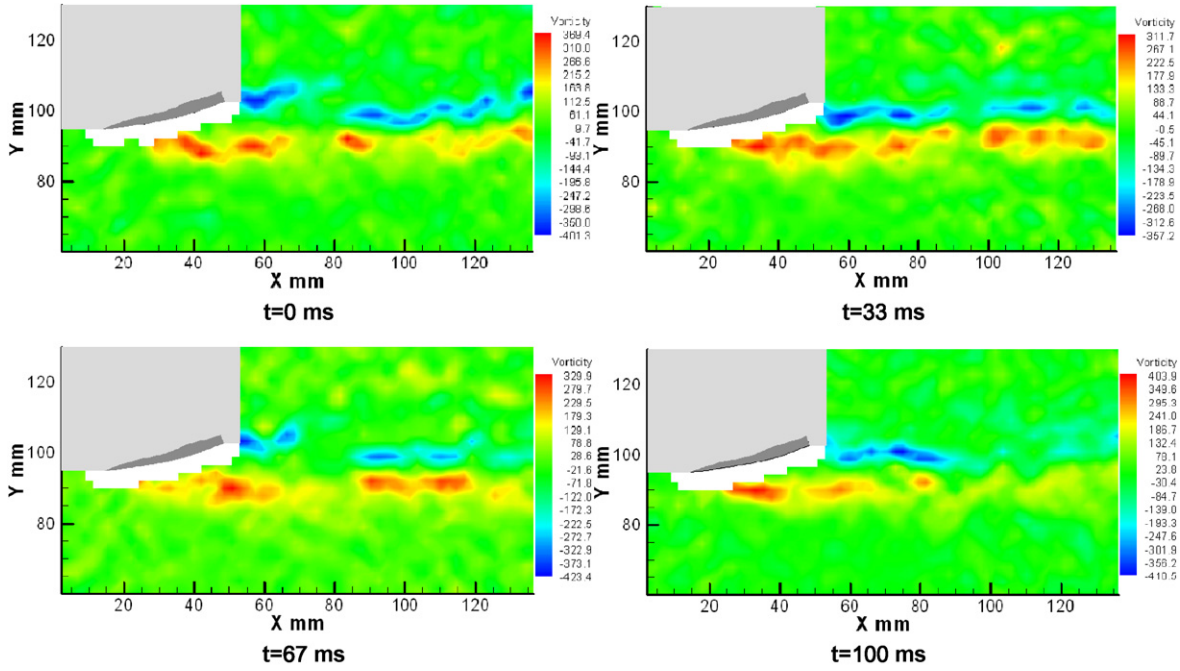

Fig. 24. Illustration of the instantaneous, z-component vorticity distribution ($\sigma = 0.26$).

be addressed based on first-principles computational modeling techniques.

Acknowledgements

The authors gratefully acknowledge support by the National Natural Science Foundation of China (NSFC, Grant No.: 50276004 and No.: 50679001) and NASA Constellation University Institutes Program.

References

[1] G.Y. Wang, I. Senocak, W. Shyy, T. Ikohagi, S.L. Cao, Dynamics of attached turbulent cavitating flows, Prog. Aerosp. Sci. 37 (2001) 551–581.
[2] E.P. Rood, Review-mechanisms of cavitation inception, J. Fluids Eng. 113 (1991) 163–175.
[3] Y. Kawanami, H. Kato, H. Yamauchi, M. Tanimura, Y. Tagaya, Mechanism and control of cloud cavitation, J. Fluids Eng. 119 (1997) 788–794.
[4] A.T. Leger, S.L. Ceccio, Examination of the flow near the leading edge of attached cavitation, part 1. Detachment of two-dimensional and axisymmetric cavities, J. Fluid Mech. 376 (1998) 61–90.
[5] D.F. Delange, G.J. Debruin, Sheet cavitation and cloud cavitation, reentrant jet and three-dimensionality, Appl. Sci. Res. 58 (1998) 91–114.
[6] M. Kjeldsen, R.E.A. Arndt, M. Effertz, Spectral characteristics of sheet/cloud cavitation, Transactions of the ASME, J. Fluids Eng. 122 (2000) 481–487.
[7] J.D. Hrubes, High-speed imaging of supercavitating underwater projectiles, Exp. Fluids 30 (2001) 57–64.
[8] R. Kuklinski, C. Henoch, J. Castano, Experimental study of ventilated cavities on dynamic test model, in: Proceedings of Fifth International Symposium on Cavitation (CAV2001), Pasadena, California, USA, 2001, Session B3.004.
[9] Y.T. Wu, D.P. Wang, A wake model for free-streamline flow theory, part 2. Cavity flows past obstacles of arbitrary profile, J. Fluid Mech. 18 (1963) 65–93.
[10] R.F. Kunz, D.R. Stinebring, T.S. Chyczewski, J.W. Lindau, H.J. Gibeling, S. Venkateswaran, T.R. Govindan, A preconditioned Navier–Stokes method for two-phase flows with application to cavitation prediction, Comput. Fluids 29 (2000) 849–875.
[11] I. Senocak, W. Shyy, A pressure-based method for turbulent cavitating flow computation, J. Comput. Phys. 176 (2002) 363–383.
[12] J.Y. Wu, G.Y. Wang, W. Shyy, Time-dependent turbulent cavitating flow computations with interfacial transport and filter-based models, Int. J. Numer. Meth. Fluids 49 (2005) 739–761.
[13] A. Hosangadi, V. Ahuja, S. Arunajatesan, A generalized compressible cavitation model, in: Proceedings of Fifth International Symposium on Cavitation (CAV2001), Pasadena, California, USA, 2001, Session B4.003.
[14] A.L. Tassin, C.Y. Li, S.L. Ceccio, L.P. Bernal, Velocity field measurements of cavitating flows, Exp. Fluids 20 (1995) 125–130.
[15] O. Claudia, S. Ceccio, The Influence of developed cavitation on the flow of a turbulent shear layer, Phys. Fluids 14 (2002) 3414–3431.
[16] S. Gopalan, J. Katz, Flow structure and modeling issues in the closure region of attached cavitation, Phys. Fluids 12 (2000) 895–911.
[17] E.J. Foeth, C.W.H. Vandoorne, T. Vantersiega, B. Wieneke, Time resolved PIV and flow visualization of 3D sheet cavitation, Exp. Fluids 40 (2006) 503–513.
[18] R.J. Adrian, Twenty years of particle image velocimetry, Exp. Fluids 39 (2005) 159–169.
[19] M.P. Tulin, Supercavitating propellers, in: Proceedings of fourth ONR Symp. on Naval Hydrodyn., ONR/ACR-92, Belgium, 2001, pp. 239–286.
[20] G. Grünefeld, H. Finke, J. Bartelheimer, S. Krüger, Probing the velocity fields of gas and liquid phase simultaneously in a two-phase flow, Exp. Fluids 29 (2000) 322–330.
[21] T. Boëdec, S. Simoëns, Instantaneous and simultaneous planar velocity field measurements of two phases for turbulent mixing of high pressure sprays, Exp. Fluids 31 (2001) 506–518.
[22] M. Wosnik, G. Lucas, R.E.A. Arndt, Measurements in high void fraction turbulent bubbly wakes created by axisymmetric ventilated supercavitation, in: Proceedings of ASME Fluids Engineering Division Summer Conference, 2005 Forums, FEDSM2005, 2005, pp. 531–538.
[23] R.T. Knapp, J.W. Daily, F.G. Hammitt, Cavitation, McGraw–Hill, New York, 1970.
[24] S.T. Johansen, J. Wu, W. Shyy, Filter-based unsteady RANS computations, Int. J. Heat Fluid Flow 25 (2004) 10–21.